

NONLOCAL MULTICONTINUA WITH REPRESENTATIVE VOLUME ELEMENTS. BRIDGING SEPARABLE AND NON-SEPARABLE SCALES

ERIC T. CHUNG, Y. EFENDIEV, WING T. LEUNG, AND M. VASILYEVA

ABSTRACT. Recently, several approaches for multiscale simulations for problems with high contrast and no scale separation are introduced. Among them is nonlocal multicontinua (NLMC) method, which introduces multiple macroscopic variables in each computational grid. These approaches explore the entire coarse block resolution and one can obtain optimal convergence results independent of contrast and scales. However, these approaches are not amenable to many multiscale simulations, where the subgrid effects are much smaller than the coarse-mesh resolution. For example, molecular dynamics of shale gas occurs in much smaller length scales compared to the coarse-mesh size, which is of orders of meters. In this case, one can not explore the entire coarse-grid resolution in evaluating effective properties. In this paper, we merge the concepts of nonlocal multicontinua methods and Representative Volume Element (RVE) concepts to explore problems with extreme scale separation. The first step of this approach is to use sub-grid scale (sub to RVE) to write a large-scale macroscopic system. We call it intermediate scale macroscale system. In the next step, we couple this intermediate macroscale system to the simulation grid model, which are used in simulations. This is done using RVE concepts, where we relate intermediate macroscale variables to the macroscale variables defined on our simulation coarse grid. Our intermediate coarse model allows formulating macroscale variables correctly and coupling them to the simulation grid. We present the general concept of our approach and present details of single-phase flow. Some numerical results are presented. For nonlinear examples, we use machine learning techniques to compute macroscale parameters.

1. INTRODUCTION

In recent years, many multiscale methods have been developed for solving challenging problems with multiple scales. Some important classes of multiscale problems include problems with scale separation and problems without scale separation and high contrast. For problems with scale separation, approaches such as homogenization [28], heterogeneous multiscale methods [15], equation free [35], and so on, are developed. These approaches explore Representative Volume Element (RVE) computations and use them to compute effective properties. To demonstrate the main idea of these approaches, we consider

$$-div\kappa(x, \nabla u) = f,$$

where $\kappa(x, \cdot)$ has a scale separation. The computational domain is divided into coarse blocks and at each coarse block (see Figure 1.1), effective property is computed by solving local problems in each RVE. These local problems are typically formulated as

$$-div\kappa(x, \nabla \mathcal{N}) = 0$$

subject to $\mathcal{N} = \xi \cdot x$, for all ξ . The effective flux is computed as the average $\kappa^*(\xi) = \langle \kappa(x, \nabla \mathcal{N}) \rangle$, where the average is taken over RVE.

The multiscale methods for problems without scale separation has been an active area of research. These methods typically explore the entire coarse block and some nearby regions to build effective properties. Some original methods in this direction include Multiscale Finite Element Method (MsFEM) [25], Generalized Multiscale Finite Element Method (GMsFEM) [16, 21, 13, 8, 14, 7], Multiscale Finite Volume [22, 26, 27], Constraint Energy Minimizing GMsFEM (CEM-GMsFEM) [9], Nonlocal Multicontinua Approaches (NLMC) [10], metric-based upscaling [34], Heterogeneous Multiscale Method [15, 1], LOD [23], equation free approaches [35, 38, 37], computational continua [19, 18, 17], hierarchical multiscale method [24, 3, 39], homogenization-based approaches [4, 30, 20, 29, 6, 5, 36], and so on. In this paper, we focus on high-contrast problems, where approaches CEM-GMsFEM [12, 9] and NLMC [10] are used to achieve

an optimal convergence independent of contrast and scales. These approaches use multiple macroscopic variables and oversampling regions to construct coarse-grid equations. Next, we briefly describe these approaches before giving main details of our proposed methods, which use concepts of RVE upscaling and multicontinua nonlocal upscaling.

We briefly describe nonlocal multicontinua approaches. In these approaches, we first identify macroscopic variables in each coarse block via local spectral decomposition. We denote them by $U_i^{(j)}$, where i is coarse-grid block and j is macroscopic variable in this coarse block. These macroscopic variables typically represent averages of solutions over some regions, which can not be localized, such as high-contrast channels in porous media applications. In the second step, we construct downscaled maps from macroscopic variables to the fine grid in the region of influence (typically oversampled regions),

$$\mathcal{R} : U_i^{(j)} \rightarrow u_f.$$

Once the maps from macroscopic variables to the fine-grid field are identified, we seek macroscopic solution (values of macroscopic variables $U_i^{(j)}$) such that the downscaled solution solves the global problem in a weak sense. We will give more detailed description later on.

The use multiple macroscopic variables are critical in multiscale simulations [10, 17]. However, our known approaches use entire coarse resolution to compute macroscale variables, which are not feasible for many applications. For example, in shale gas applications, gas dynamics is described by molecular dynamics of multi-component gas particles. The local simulations are only possible in small RVEs; however, one needs to perform large-scale simulations for predicting flow in reservoirs. In this paper, we couple RVE simulations and nonlocal multicontinua approaches to develop efficient numerical simulations, where we can partly explore the scale separation ideas. These problems can occur in many applications, where intermediate scales are used to get very large systems and then, explore RVE concepts. Next, we briefly describe these ideas.

We assume that there are three macroscopic scales. The first scale is denoted by h and can be regarded as a scale, where we apply nonlocal multicontinua approach and write down an intermediate macroscale equations for $U_i^{(j)}$,

$$G_h(U_i^{(j)}) = 0.$$

These equations are nonlocal and very expensive to solve. In the next step, we use RVE ideas to connect these variables to macroscale variables $\bar{U}_i^{(j)}$ defined on H -size grid, where we perform computations. We introduce an intermediate coarse-mesh scale, RVE scale, denoted by H_{RVE} , and assume $h \ll H_{RVE} \ll H$. In the next step, we use RVE computations to connect $U_i^{(j)}$ to $\bar{U}_i^{(j)}$,

$$U_i^{(j)} = \mathcal{R}(\bar{U}).$$

This is done via solving RVE problems subject to some constraints that use \bar{U} . Once we define the map, we perform quadrature of macroscale equations using RVE cells (cf., [15]).

In the proposed approaches, we make two major assumptions. Though the equations on h -scale are rigorous, their connections to H -scale equations require (1) periodicity (2) identifying macroscale variables. As for periodicity assumptions, our approaches are similar to existing methods, such as HMM, equation free, and so on. However, defining macroscale variables on h -scale and using similar macroscopic variables on H -scale is one of main advantages, which allow introducing macroscale variables in a rigorous fashion.

In the paper, we give an overview of our approach. Our approach relies on NLMC approach, and for this reason, we first present this approach. We describe steps of our approach and then give a detailed study for linear system. We present some convergence result under certain assumptions. We also obtain a PDE description of our macroscale equations, which has integro-differential form. We present some numerical results.

The paper is organized as follows. In Section 2, we present a general concept. Section 3 is devoted to detailed studies of the linear case. Finally, in Section 4, we present some numerical results.

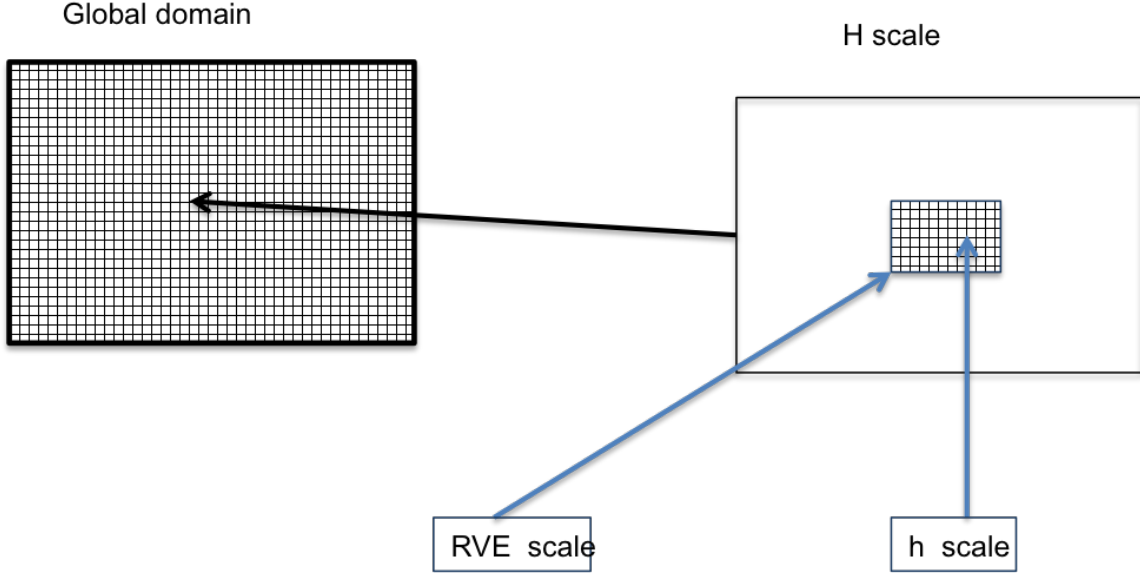


FIGURE 1.1. Schematic description of the grids

2. GENERAL CONCEPT

2.1. **NLNLNC on RVE-scale.** We will first follow [11, 31] and present nonlinear NLNC on RVE scale using the following model nonlinear problem

$$(2.1) \quad MU_t + \nabla \cdot G(x, t, U) = g,$$

where G is a nonlinear operator that has a multiscale dependence with respect to space (and time, in general) and M is a linear operator. In the above equation, U is the solution and g is a given source term. In this part, we use the approach proposed in [11, 31] on RVE scale, which is expensive and then apply homogenization idea.

- **The choice of continua**

The continua serves as our macroscopic variables in each coarse element. Our approach uses a set of test functions to define the continua. To be more specific, we consider a coarse element K_i . We will choose a set of test functions $\{\psi_i^{(j)}(x, t)\}$ to define our continua, where j denotes the j -th continuum. Using these test functions, we can define our macroscopic variables as

$$U_i^{(j)} = \langle\langle U, \psi_i^{(j)} \rangle\rangle$$

where $\langle\langle \cdot, \cdot \rangle\rangle$ is a space-time inner product.

- **The construction of local downscaling map**

Our upscale model uses a local downscaling map to bring microscopic information to the coarse grid model. The proposed downscaling map is a function defined on an oversampling region subject to some constraints related to the macroscopic variables. More precisely, we consider a coarse element K_i , and an oversampling region K_i^+ such that $K_i \subset K_i^+$. Then we find a function ϕ by solving the following local problem

$$(2.2) \quad M\phi_t + \nabla \cdot G(x, t, \phi) = \mu, \quad \text{in } K_i^+.$$

The above equation (2.2) is solved subjected to constraints defined by the following functionals

$$I_\phi(\psi_i^{(j)}(x, t)).$$

This constraint fixes some averages of ϕ with respect to $\psi_i^{(j)}(x, t)$. We remark that the function μ serves as the Lagrange multiplier for the above constraints. This local solution builds a

downscaling map

$$\mathcal{F}_i^{ms} : I_\phi(\psi_i^{(j)}(x, t)) \rightarrow \phi.$$

- **The construction of coarse scale model**

We will construct the coarse scale model using the test functions $\{\psi_i^{(j)}(x, t)\}$ and the local downscaling map. Our upscaling solution U^{ms} is defined as a combination of the local downscaling maps. To compute U^{ms} , we use the following variational formulation

$$(2.3) \quad \langle \langle MU_t^{ms} + \nabla \cdot G(x, t, U^{ms}), \psi_i^{(j)} \rangle \rangle = \langle \langle g, \psi_i^{(j)} \rangle \rangle.$$

The above equation (2.3) is our coarse scale model.

2.2. RVE-based NLNLMC. We denote by H the coarse-mesh size, where the final computations are performed. We denote by h a scale, where we write nonlocal multicontinua equations; however, they are very large to solve and will be reduced to H -scale. We denote H_{RVE} , the scale of RVE and it is assumed $H \gg H_{RVE} \gg h$. There is also very fine grid, which is subgrid of h .

- First, we note that in NLNLMC, we find $U_i^{(j)}$ (on h -scale) such that

$$(2.4) \quad \langle \langle MU_t^{ms} + \nabla \cdot G(x, t, U^{ms}), \psi_i^{(j)} \rangle \rangle = \langle \langle g, \psi_i^{(j)} \rangle \rangle,$$

where U^{ms} depends on $U_i^{(j)}$, which are defined on h -scale. This equation is very large and we will only use RVE-based solution.

- Our second goal is to use RVE concept and reduce the dimension of $U_i^{(j)}$. We introduce a coarse-grid homogenized solution and denote it by \bar{U}^H (defined on H -scale) and write its finite element expansion

$$\bar{U}^H = \sum_{i,j} \bar{U}_i^{(j)} \bar{\Phi}_i^j,$$

where $\bar{\Phi}_i^j$ are standard basis functions, for example, piecewise linear on H -scale. We seek a reduced map

$$U_i^{(j)} = \mathcal{R}_H(\bar{U}).$$

This map can be local or nonlocal, in general. Our construction is based on homogenization ideas and uses local maps, which we introduce next. Using these local maps, the quadrature can be approximated on RVEs. In a linear case, \mathcal{R} is a matrix of the sizes corresponding to H^{-d} and h^{-d} .

In the simplest approach, we will use \mathcal{R}_H to be L^2 projection of \bar{U}^H (i.e., the averages of \bar{U}^H on h -scale mesh).

- There are various ways to use homogenization ideas to construct reduced map. Here, we consider some of them, which differ in a way we impose constraints.

Approach 1. In this approach, we solve RVE-based local problem with constraints given by \bar{U}^H on each RVE cell to define a map \mathcal{R}_h^K , which is local for each coarse block.

Approach 2. In this approach, we solve local problems on RVE (H_{RVE} -scale) subject to boundary conditions U^H (to be determined)

$$(2.5) \quad M\phi_t + \nabla \cdot G(x, t, \phi) = \mu, \quad \text{in } K_i^{RVE}$$

subject to boundary condition and initial condition at $t = t_n$

$$\phi = \mathcal{R}_H(\bar{U}^H),$$

where $\phi = \mathcal{R}_h(\mathcal{R}_H(\bar{U}^H))$. This equation gives a map between the local solution and $\mathcal{R}_H(\bar{U}^H)$. Next, we define

$$\langle \phi, \psi_i^{(j)} \rangle,$$

and the map

$$\langle \phi, \psi_i^{(j)} \rangle = \mathcal{R}_H(\bar{U}_i^{(j)}).$$

The map \mathcal{R}_h can be regarded as a reduced dimensional map mentioned in the previous step.

- In the last step, we discuss the approximation of the integrals defined in coarse-grid system and the coarse-grid system. We seek \bar{U} such that

$$\langle \langle M\mathcal{R}_h(\mathcal{R}_H(\bar{U}))_t + \nabla \cdot G(x, t, \mathcal{R}_h(\mathcal{R}_H(\bar{U}))), \psi_i^{(j)} \rangle \rangle_{RVE} = \langle \langle g, \psi_i^{(j)} \rangle \rangle_{RVE},$$

where $\psi_i^{(j)}$ are standard (e.g., linear test functions).

2.3. Examples. *Example 1.* We consider

$$-div\kappa(x, \nabla u) = f,$$

where $\kappa(x, \xi)$ is monotone with respect to ξ (see [31]). The algorithm is the following. We seek $\bar{U}^H = \sum_{i,j} \bar{U}_i^{(j)} \bar{\Phi}_i^j$, such that

$$\int_{\Omega} \kappa(x, \nabla \mathcal{R}_h^K(\mathcal{R}_H(\bar{U}))) \cdot \bar{\Phi}_i^j dx = \int_{\Omega} f \bar{\Phi}_i^j dx,$$

where $\mathcal{R}_H(\bar{U})$ is L^2 projection of \bar{U} onto h -size mesh in RVE, and $\mathcal{R}_h(\mathcal{R}_H(\bar{U}))$ is the local RVE solution defined on the fine grid with constraints given by $\mathcal{R}_H(\bar{U})$ (which is defined on h -size mesh),

$$\begin{aligned} \int_{\Omega} \kappa(x, \nabla \mathcal{R}_h(\mathcal{R}_H(\bar{U}))) \cdot \bar{\Phi}_i^j dx &\approx \sum_K \omega_K \int_{K_{RVE}} \kappa(x, \nabla \mathcal{R}_h^K(\mathcal{R}_H(\bar{U}))) \cdot \bar{\Phi}_i^j dx \\ \int_{\Omega} f \bar{\Phi}_i^j dx &\approx \sum_K \omega_K \int_{K_{RVE}} f \bar{\Phi}_i^j dx. \end{aligned}$$

We again note that \mathcal{R}_h^K is local map, $\mathcal{R}_h^K : V_h(K_{RVE}) \rightarrow V(K_{RVE})$, and $\mathcal{R}_H : V_H \rightarrow \oplus_K V_h(K_{RVE})$ couples different coarse regions.

Example 2. We consider a simpler example

$$-div(\kappa(x, u)\nabla u) = f.$$

In this case, we can consider a linearization (Picard) as

$$-div(\kappa(x, u^n)\nabla u^{n+1}) = f.$$

Then, the algorithm is a special case of *Example 1*. We seek \bar{U}^{n+1} , which solves the linearized equations. In this case, we can also define effective permeabilities as we will do in our numerical examples.

3. DETAILED STUDY OF LINEAR CASE

In this section, we will discuss a linear case in detail. We consider the following variational problem: find $u_\epsilon \in V$ such that

$$(3.1) \quad a_\epsilon(u_\epsilon, v) = \int_{\Omega} f v, \quad \forall v \in V,$$

where $a_\epsilon : V \times V \rightarrow \mathbb{R}$ is a bilinear form, ϵ is the size of the microscopic scale, V is a Hilbert space which is compactly embedded in $L^2(\Omega)$, f is a source function in $L^2(\Omega)$ and Ω is the computational domain in \mathbb{R}^d . Before introducing our NLMC upscaling method, we will first define the macroscopic quantities for the solution u_ϵ . We assume that there is a set of weighted functions, denoted by $\{\phi_j^{h,\epsilon}(y, x)\}$, which can capture the major features of the solution. Under this assumption, we can define a macroscopic system to compute the macroscopic quantities of the solution. In the following subsections, we will construct the upscaled bilinear operators \tilde{a}_{ij} such that the solution $u_j \in V_j$ with $u_j(x) \approx \int_{\Omega} \phi_j^{h,\epsilon} u_\epsilon(y, x) dy$ satisfies

$$(3.2) \quad \sum_j \tilde{a}_{ij}(u_j, v_i) = \int_{\Omega} f v_i, \quad \forall v_i \in V_i.$$

By using these equations, we can construct a Galerkin method to compute the numerical solution. Let \mathcal{T}_H be a partition of Ω . We consider finite element spaces $V_{H,i} \subset V_i$. For example, we can take $V_{H,i}$ to be

the piecewise linear finite element space. The numerical solution $u_{H,i} \in V_{H,i}$ is then computed by solving the following equations

$$(3.3) \quad \sum_j \tilde{a}_{ij}(u_{H,j}, v_i) = \int_{\Omega} f v_i, \quad \forall v_i \in V_{H,i}.$$

To reduce the computational cost of the method, we will compute the approximate bilinear operators a_{ij}^{RVE} where $a_{ij}^{RVE} \approx \tilde{a}_{ij}$ by using our proposed RVE concept.

3.1. Construction of the upscaled system. In this section, we will introduce the construction of the upscaled bilinear operator \tilde{a}_{ij} . Let \mathcal{T}_h be a partition of Ω where h is the mesh size of \mathcal{T}_h . This h is chosen to be the intermediate scale size which is smaller than the RVE size but larger than the microscopic feature size. In the following discussions, we will consider \mathcal{T}_h to be the partition

$$\mathcal{T}_h = \{K \mid K = \left(x_0 + nh + \left[-\frac{h}{2}, \frac{h}{2}\right]\right) \cap \Omega \text{ for } n \in \mathbb{Z}^d\}$$

where x_0 is a point in Ω . We remark that, in the RVE case, we construct the partition locally in the RVE and x_0 can be chosen to be the center of the RVE. Next, we use the function $\psi_j^{h,\epsilon}(x, y)$ to represent the j -th continuum for the local region $K(x) = \left(x + \left[-\frac{h}{2}, \frac{h}{2}\right]^d\right) \cap \Omega$ with

$$\sum_j \omega_j^{h,\epsilon}(x) \psi_j^{h,\epsilon}(x, \cdot) = \frac{(\tilde{\kappa}^\epsilon)^{-1}}{|K(x)|} I_{K(x)}$$

and

$$\int_{\Omega} \tilde{\kappa}^\epsilon(y) \psi_k^{h,\epsilon}(x, y) \psi_j^{h,\epsilon}(x, y) dy = \delta_{jk}$$

where $\tilde{\kappa}^\epsilon \in L^\infty$ is a weight function with $\tilde{\kappa}^\epsilon \geq \alpha_0 > 0$. Next, we define $J^h(x) = \{y \in \Omega, y_i = x_i + n_i h, n \in \mathbb{Z}^d\}$, where x_i denotes the i -th component of x . By solving the local problem, we obtain basis functions $\phi_j^{h,\epsilon}(x, \cdot) \in V$ and $\mu_j^{h,\epsilon}(x, \cdot) \in V_{aux}^h := \text{span}_{z \in J^h(x)} \{\psi_k^{h,\epsilon}(z, \cdot)\}$ as

$$a_\epsilon(\phi_j^{h,\epsilon}(x, \cdot), v) = \int_{\Omega} \tilde{\kappa}^\epsilon(y) \mu_j^{h,\epsilon}(x, y) v(y) dy, \quad \forall v \in V,$$

$$\int_{\Omega} \tilde{\kappa}^\epsilon(y) \phi_j^{h,\epsilon}(x, y) \psi_k^{h,\epsilon}(z, y) dy = \delta(x, z) \delta_{jk}, \quad \forall z \in J^h(x),$$

where a_ϵ is a symmetric positive bilinear operator with $a_\epsilon(u, u) \geq \alpha \|u\|_{L^2(\Omega)}^2$, $\forall \epsilon > 0$. For example, $a_\epsilon(\phi, v) = \int_{\Omega} \kappa(\epsilon, y) \nabla \phi(y) \cdot \nabla v(y) dy$.

We define $\tilde{u}^{h,\epsilon}(x_0, y) = \sum_{x \in J(x_0)} \sum_j u_j^{h,\epsilon}(x_0, x) \phi_j^{h,\epsilon}(x, y)$ as

$$(3.4) \quad a_\epsilon \left(\sum_{x \in J^h(x_0)} \sum_j u_j^{h,\epsilon}(x_0, x) \phi_j^{h,\epsilon}(x, \cdot), \phi_k^{h,\epsilon}(z, \cdot) \right) = \int_{\Omega} f(y) \phi_k^{h,\epsilon}(z, y) \quad \forall z \in J^h(x_0).$$

By the definition of $\phi_j^{h,\epsilon}(x, y)$, we have

$$a_\epsilon \left(\sum_{x \in J^h(x_0)} \sum_j u_j^{h,\epsilon}(x_0, x) \phi_j^{h,\epsilon}(x, \cdot), v(\cdot) \right) = \int_{\Omega} \tilde{f}^{h,\epsilon}(x_0, y) v(y) dy, \quad \forall v \in V,$$

where $\tilde{f}_k^{h,\epsilon}(x_0, y) = \sum_{z \in J^h(x_0)} f_k(z) \tilde{\kappa}^\epsilon(y) \psi_k^{h,\epsilon}(z, y)$ and $f_k(z) = \int_{\Omega} f(y) \phi_k^{h,\epsilon}(z, y)$.

It is clear that for all x_0 , we have $\tilde{u}^{h,\epsilon}(x_0, \cdot) \in V$ and $\tilde{f}_k^{h,\epsilon}(x_0, \cdot) \in L^2(\Omega)$. Using the idea in [12], we have

$$\|\tilde{u}^{h,\epsilon}(x_0, \cdot) - u^\epsilon\|_a \leq C^\epsilon(h), \quad \forall x_0,$$

and

$$\int_{\Omega} u_j^{h,\epsilon}(x_0, x) \psi_j^{h,\epsilon}(x, \cdot) = \int_{\Omega} u^\epsilon(y) I_{K(x)}(y), \quad \forall x \in J^h(x_0).$$

To simplify the notation, we will consider a fixed x_0 and neglect the index x_0 , for example,

$$u_j^{h,\epsilon}(x) = u_j^{h,\epsilon}(x_0, x).$$

In addition, we define two different norms $\|\cdot\|_{a,\epsilon}$ and $\|\cdot\|_{s,\epsilon}$ as

$$\|u\|_{a,\epsilon}^2 = a_\epsilon(u, u),$$

$$\|u\|_{s,\epsilon}^2 = \|u\|_{L^2(\tilde{\kappa}, \Omega)}^2 = \int_{\Omega} \tilde{\kappa}^\epsilon \mu^2.$$

Definition 1. We define a restriction operator $R_{0,k}^h : L^2(\Omega) \rightarrow l^2(J^h(x_0))$ and two prolongation operators $P_{0,k}^h : l^2(J^h(x_0)) \rightarrow L^2(\Omega)$, $P_{1,k}^h : l^2(J^h(x_0)) \rightarrow V$ by

$$\left(R_{0,k}^h(u)\right)(z) = \int_{\Omega} \tilde{\kappa}(y) u(y) \psi_k^{h,\epsilon}(z, y) dy$$

$$P_{0,k}^h(v) = \sum_{z \in J^h(x_0)} v(z) \psi_k^{h,\epsilon}(z, y)$$

and

$$P_{1,k}^h(v) = \sum_{z \in J^h(x_0)} v(z) \phi_k^{h,\epsilon}(z, y)$$

Moreover, we define an operator $\Pi_k^h : L^2(\Omega) \rightarrow L^2(\Omega)$ such that $\Pi_k^h = P_{0,k}^h \circ R_{0,k}^h$. We can easily check that $\sum_k \Pi_k^h(u) = u$ for all $u \in \text{span}_{z \in J^h(x)} \{\psi_k^{h,\epsilon}(z, \cdot)\}$.

Next, we make the following assumption.

Assumption 1: For all $\mu \in \text{span}_{z \in J^h(x)} \{\psi_k^{h,\epsilon}(z, \cdot)\}$, there exists $v \in V$ with $\text{supp}\{v\} \subset \text{supp}\{\mu\}$ such that

$$\int_{\Omega} \tilde{\kappa}^\epsilon \mu v \geq c^\epsilon(h) \left(\int_{\Omega} \tilde{\kappa}^\epsilon \mu^2 \right)^{\frac{1}{2}} \left(a_\epsilon(v, v) \right)^{\frac{1}{2}}$$

and

$$\left(\int_{\Omega} \tilde{\kappa}^\epsilon \left| (I - \Pi_k^h) u \right|^2 \right)^{\frac{1}{2}} \leq C^\epsilon(h) \left(a_\epsilon(v, v) \right)^{\frac{1}{2}}$$

where C^ϵ, c^ϵ are monotonic decreasing functions with respect to ϵ . We also assume that there is a function $\beta : \mathbb{R} \rightarrow \mathbb{R}$ such that $C^\epsilon(\beta(\epsilon)) \rightarrow 0$ and $\beta(\epsilon) \rightarrow 0$.

We next prove the following properties for the operators $R_{0,k}^h, P_{0,k}^h$ and $P_{1,k}^h$.

Lemma 2. For the operators $R_{0,k}^h, P_{0,k}^h$ and $P_{1,k}^h$ defined in **Definition 1**, the following hold

$$\|R_{0,k}^h\|_{L^2(\tilde{\kappa})} = 1,$$

$$\|P_{0,k}^h(v)\|_{L^2(\Omega)} = \|v\|_{l^2}, \quad \forall v \in l^2(J^h(x_0)),$$

$$\|P_{1,k}^h(v)\|_{a,\epsilon} \leq c^\epsilon(h)^{-1} \|v\|_{l^2}, \quad \forall v \in l^2(J^h(x_0)).$$

In addition, we have

$$\|P_{1,k}^h \circ R_{0,k}^h(u)\|_{a,\epsilon} \leq \|u\|_{a,\epsilon}, \quad \forall u \in V.$$

Proof. By the orthogonality of $\psi_k^{h,\epsilon}(z, \cdot)$, we obtain the first two inequalities. For the third inequality, we note that $P_{1,k}^h(u)$ satisfies

$$a_\epsilon(P_{1,k}^h(u), v) = \sum_{j,z} \mu_j(z) \int_{\Omega} \tilde{\kappa}^\epsilon \psi_j^{h,\epsilon}(z, y) v(y) dy, \quad \forall v \in V,$$

$$\int_{\Omega} \tilde{\kappa}^\epsilon P_{1,k}^h(u) \psi_j^{h,\epsilon}(z, y) dy = \delta_{jk} u(z), \quad \forall z \in J^h(x).$$

Therefore, we have

$$\begin{aligned} a_\epsilon(P_{1,k}^h(u), P_{1,k}^h(u)) &= \sum_{j,z} \mu_j(z) \int_{\Omega} \tilde{\kappa}^\epsilon \psi_j^{h,\epsilon}(z, y) P_{1,k}^h(u) dy \\ &= \sum_z \mu_k(z) u(z) \leq \|\mu_k\|_{l^2} \|u\|_{l^2}. \end{aligned}$$

By **Assumption 1**, there is $v \in V$ such that

$$\sum_z \mu_k(z) \int_{\Omega} \tilde{\kappa}^\epsilon \psi_k^{h,\epsilon}(z, y) v dy \geq c^\epsilon(h) \left\| \sum_z \mu_k(z) \psi_k^{h,\epsilon}(z, \cdot) \right\|_{s,\epsilon} \|v\|_{a,\epsilon} = c^\epsilon(h) \|\mu_k\|_{l^2} \|v\|_{a,\epsilon},$$

so, we have

$$\begin{aligned} \|\mu_k\|_{l^2} &\leq \frac{\sum_z \mu_k(z) \int_{\Omega} \tilde{\kappa}^\epsilon \psi_k^{h,\epsilon}(z, y) v dy}{c^\epsilon(h) \|v\|_{a,\epsilon}} \\ &= \frac{a_\epsilon(P_{1,k}^h(u), v)}{c^\epsilon(h) \|v\|_{a,\epsilon}} \leq c^\epsilon(h)^{-1} \|P_{1,k}^h(u)\|_{a,\epsilon}. \end{aligned}$$

To obtain the fourth inequality, we note that $P_{1,k}^h \circ R_{0,k}^h(u)$ is the solution of the following minimization problem

$$P_{1,k}^h \circ R_{0,k}^h(u) = \operatorname{argmin}_{v \in V} \{a_\epsilon(v, v) \mid R_{0,k}^h(v) = R_{0,k}^h(u)\}.$$

This completes the proof of the lemma. \square

The following lemma gives an error estimate for $\tilde{u}^{h,\epsilon}$ defined in (3.4).

Lemma 3. *For the function $\tilde{u}^{h,\epsilon}$ defined in (3.4), we have*

$$\|\tilde{u}^{h,\epsilon} - u^\epsilon\|_{a,\epsilon} = \left\| \sum_k P_{1,k}^h \circ R_{0,k}^h(u^\epsilon) - u^\epsilon \right\|_{a,\epsilon} \leq C^\epsilon(h) \|(\kappa^\epsilon)^{-\frac{1}{2}} f\|_{L^2(\Omega)}$$

and

$$\left\| \sum_{x \in J^h} u_j^{h,\epsilon}(x) \psi_j^{h,\epsilon}(x, \cdot) - u^\epsilon \right\|_{s,\epsilon} = \left\| \sum_k \Pi_k^h(u^\epsilon) - u^\epsilon \right\|_{s,\epsilon} \leq C^\epsilon(h) \|u^\epsilon\|_{a,\epsilon}.$$

Proof. The first inequality is obtained by the concepts developed in [12]. The second inequality is a direct consequence of **Assumption 1**. \square

Now, we present our upscaled quantities.

Definition 4. We define $\bar{\kappa}_{jk}^{h,\epsilon}$ and $\tilde{\kappa}_{jk}^{h,\epsilon}$ as

$$\bar{\kappa}_{jk}^{h,\epsilon}(x, z) = a_\epsilon(\phi_j^{h,\epsilon}(x, \cdot), \phi_k^{h,\epsilon}(z, \cdot)), \quad \forall x, y \in J^h,$$

and

$$\tilde{\kappa}_{jk}^{h,\epsilon}(x, z) = \sum_{\tilde{x} \in J} \sum_{\tilde{z} \in J} \psi_j^{h,\epsilon}(\tilde{x}, x) \bar{\kappa}_{jk}^{h,\epsilon}(\tilde{x}, \tilde{z}) \psi_k^{h,\epsilon}(\tilde{z}, z).$$

We remark that for all $u, v \in L^2(\Omega)$, we have

$$\int_{\Omega} \int_{\Omega} v(z) \tilde{\kappa}^\epsilon(z) \tilde{\kappa}_{jk}^{h,\epsilon}(x, z) \tilde{\kappa}^\epsilon(x) u(x) = \sum_{x,z \in J} R_{0,k}^h(u)(x) \bar{\kappa}_{jk}^{h,\epsilon}(x, z) R_{0,j}^h(v)(x).$$

Thus we have

$$\sum_j \int_{\Omega} \int_{\Omega} v(y) \tilde{\kappa}^\epsilon(y) \tilde{\kappa}_{jk}^{h,\epsilon}(x, y) \tilde{\kappa}^\epsilon(x) \tilde{u}^{h,\epsilon}(x) = \int_{\Omega} \tilde{f}_k^{h,\epsilon}(x_0, y) v(y) dy, \quad \forall v \in V.$$

Using $R_{0,j}^h(\tilde{u}^{h,\epsilon}(x)) = R_{0,j}^h(u^\epsilon(x))$, we obtain

$$\sum_j \int_{\Omega} \int_{\Omega} v(y) \tilde{\kappa}^\epsilon(y) \tilde{\kappa}_{jk}^{h,\epsilon}(x, y) \tilde{\kappa}^\epsilon(x) u^\epsilon(x) = \int_{\Omega} \tilde{f}_k^{h,\epsilon}(y) v(y) dy, \quad \forall v \in V.$$

We remark that the bilinear operator $\tilde{a}^{h,\epsilon}$ defined as

$$\tilde{a}^{h,\epsilon}(u, v) := \int_{\Omega} \int_{\Omega} v(y) \tilde{\kappa}^{\epsilon}(y) \tilde{\kappa}_{jk}^{h,\epsilon}(x, y) \tilde{\kappa}^{\epsilon}(x) \tilde{u}^{h,\epsilon}(x)$$

is not positive neither in $L^2(\Omega)$ nor in V . On the other hand, one can easily prove that the bilinear operator $\tilde{a}^{h,\epsilon}$ is positive in V_{aux}^h and $V^h = \text{span}\{\phi_j^{h,\epsilon}\}$ where $\cup_{j=1}^{\infty} V_{aux}^{h_j} = L^2(\Omega)$, $\cup_{j=1}^{\infty} V^{h_j} \subset V$ for any sequence $h_j \rightarrow 0$.

For the next result, we make the following assumptions.

Assumption 2: We assume that, there exist \tilde{V} such that for all $f \in L^2(\Omega)$, the solution $\Pi_k^{\beta(\epsilon)} u^{\epsilon} \rightarrow u_k^0$ in $L^2(\Omega)$ and $u_k^0 \in \tilde{V}_k$ satisfies

$$\sum_k a_{j,k}^0(u_k^0, v_j) = (f_j^0, v_j), \quad \forall v \in \tilde{V}_j,$$

for some f_j^0 .

Assumption 3: We assume that, there exist \tilde{V} such that for all $f \in L^2(\Omega)$, $\Pi_k^{\beta(\epsilon)} \tilde{u}^{\beta(\epsilon),\epsilon} \rightarrow \tilde{u}_k^0$ in $L^2(\Omega)$ and $\tilde{u}_k^0 \in \tilde{V}_k$ satisfies

$$\sum_k \tilde{a}_{j,k}^0(\tilde{u}_k^0, v_j) = (\tilde{f}_j^0, v), \quad \forall v \in \tilde{V}_j,$$

for some \tilde{f}_j^0 .

Lemma 5. *Assumption 2 holds if and only if Assumption 3 holds.*

Proof. We assume **Assumption 2** holds. First, we let $\tilde{u}_k^0 = u_k^0$ and obtain

$$\begin{aligned} \|\Pi_k^{\beta(\epsilon)}(\tilde{u}^{h,\epsilon}) - \tilde{u}_k^0\|_{L^2(\Omega)} &= \|\Pi_k^{\beta(\epsilon)}(\tilde{u}^{h,\epsilon}) - u_k^0\|_{L^2(\Omega)} \\ &\leq \|\Pi_k^{\beta(\epsilon)}\tilde{u}^{h,\epsilon} - \Pi_k^{\beta(\epsilon)}u^{\epsilon}\|_{L^2(\Omega)} + \|\tilde{u}_k^0 - \Pi_k^{\beta(\epsilon)}u^{\epsilon}\|_{L^2(\Omega)} \\ &= \|\tilde{u}_k^0 - \Pi_k^{\beta(\epsilon)}u^{\epsilon}\|_{L^2(\Omega)} \rightarrow 0. \end{aligned}$$

We consider $\tilde{a}_{j,k}^0(u, v) = a_{j,k}^0(u, v) \forall u \in \tilde{V}_k, v \in \tilde{V}_j$ and $\tilde{f}_j^0 = f_j^0$. Therefore, we obtain

$$\begin{aligned} \sum_k \tilde{a}_{j,k}^0(\tilde{u}_k^0, v_j) &= \sum_k a_{j,k}^0(u_k^0, v_j) = (f_j^0, v_j) \\ &= (\tilde{f}_j^0, v_j) \end{aligned}$$

for all $v \in \tilde{V}_j$. The statement that **Assumption 3** implies **Assumption 2** can be proved by a similar argument. \square

Our final error estimate is based on the following assumption.

Assumption 4: We assume that there exists a bilinear form $\tilde{a}_{jk} : \tilde{V}_k \times \tilde{V}_j \rightarrow \mathbb{R}$ such that

$$\frac{|\tilde{a}_{jk}(u, v) - \tilde{a}_{jk}^{\beta_0(\epsilon),\epsilon}(u, v)|}{\|u\|_{\tilde{V}_k} \|v\|_{\tilde{V}_j}} \rightarrow 0$$

where we define

$$\tilde{a}_{jk}^{h,\epsilon}(u, v) := \int_{\Omega} \int_{\Omega} v(y) \tilde{\kappa}^{\epsilon}(y) \tilde{\kappa}_{jk}^{h,\epsilon}(x, y) \tilde{\kappa}^{\epsilon}(x) u(x).$$

Furthermore, we assume there are constants c_0, c_1 and C_1 such that

$$c_0 \sum_k \|u_k\|_{L^2}^2 \leq c_1 \sum_k \|u_k\|_{\tilde{V}_k}^2 \leq \sum_{j,k} \tilde{a}_{jk}(u_k, u_j),$$

and

$$\sum_{j,k} \tilde{a}_{jk}(u_k, v_j) \leq C_1 \left(\sum_k \|u_k\|_{\tilde{V}_k}^2 \right)^{\frac{1}{2}} \left(\sum_k \|u_k\|_{\tilde{V}_k}^2 \right)^{\frac{1}{2}}.$$

We also assume that

$$\tilde{f}_j^{\beta_0(\epsilon),\epsilon} = \int_{\Omega} f(y) \sum_{z \in \mathcal{J}^h} \phi_k^{h,\epsilon}(z, y) \tilde{\kappa}^\epsilon(x) \psi_k^{h,\epsilon}(z, x) \rightarrow \tilde{f}_j.$$

We state our main result.

Theorem 1. *If Assumption 4 holds, we have $\Pi_k^{\beta_0(\epsilon)} \tilde{u}^{\beta_0(\epsilon),\epsilon} \rightarrow \tilde{u}_k$ where $\tilde{u}_k \in \tilde{V}_k$ satisfies*

$$\sum_k \tilde{a}_{j,k}(\tilde{u}_k, v_j) = (\tilde{f}_j, v_j).$$

Proof. First, we have

$$\sum_k \tilde{a}_{jk}^{\beta_0(\epsilon),\epsilon}(\Pi_k^{\beta_0(\epsilon)} \tilde{u}^{\beta_0(\epsilon),\epsilon}, v_j) = (\tilde{f}_j^{\beta_0(\epsilon),\epsilon}, v_j)$$

and, using Assumption 4,

$$\begin{aligned} c_1 \sum_k \|\Pi_k^{\beta_0(\epsilon)} \tilde{u}^{\beta_0(\epsilon),\epsilon}\|_{\tilde{V}_k}^2 &\leq \sum_{j,k} \tilde{a}_{jk}(\Pi_k^{\beta_0(\epsilon)} \tilde{u}^{\beta_0(\epsilon),\epsilon}, \Pi_j^{\beta_0(\epsilon)} \tilde{u}^{\beta_0(\epsilon),\epsilon}) \\ &\leq \sum_j \left\{ \left| \sum_k \tilde{a}_{jk}(\Pi_k^{\beta_0(\epsilon)} \tilde{u}^{\beta_0(\epsilon),\epsilon}, \Pi_j^{\beta_0(\epsilon)} \tilde{u}^{\beta_0(\epsilon),\epsilon}) - \sum_k \tilde{a}_{jk}^{\beta_0(\epsilon),\epsilon}(\Pi_k^{\beta_0(\epsilon)} \tilde{u}^{\beta_0(\epsilon),\epsilon}, \Pi_j^{\beta_0(\epsilon)} \tilde{u}^{\beta_0(\epsilon),\epsilon}) \right| \right. \\ &\quad \left. + |(\tilde{f}_j^{\beta_0(\epsilon),\epsilon}, \Pi_j^{\beta_0(\epsilon)} \tilde{u}^{\beta_0(\epsilon),\epsilon})| \right\}. \end{aligned}$$

When ϵ is small enough, we have

$$\sum_j \left| \sum_k \tilde{a}_{jk}(\Pi_k^{\beta_0(\epsilon)} \tilde{u}^{\beta_0(\epsilon),\epsilon}, \Pi_j^{\beta_0(\epsilon)} \tilde{u}^{\beta_0(\epsilon),\epsilon}) - \sum_k \tilde{a}_{jk}^{\beta_0(\epsilon),\epsilon}(\Pi_k^{\beta_0(\epsilon)} \tilde{u}^{\beta_0(\epsilon),\epsilon}, \Pi_j^{\beta_0(\epsilon)} \tilde{u}^{\beta_0(\epsilon),\epsilon}) \right| \leq \frac{c_1}{2} \|u\|_{\tilde{V}_k} \|v\|_{\tilde{V}_j}$$

and

$$\sum_k \|\Pi_k^{\beta_0(\epsilon)} \tilde{u}^{\beta_0(\epsilon),\epsilon}\|_{\tilde{V}_k}^2 \leq C \sum_j \|\tilde{f}_j^{\beta_0(\epsilon)}\|_{L^2(\Omega)}^2 \leq C \sum_j \|\tilde{f}_j\|_{L^2(\Omega)}^2.$$

Let $\eta_j = \tilde{u}_j - \Pi_j^{\beta_0(\epsilon)} \tilde{u}^{\beta_0(\epsilon),\epsilon}$. Then we have

$$\begin{aligned} c_1 \sum_k \|\eta_k\|_{\tilde{V}_k}^2 &\leq \sum_{k,j} \tilde{a}_{jk}(\tilde{u}_k - \Pi_k^{\beta_0(\epsilon)} \tilde{u}^{\beta_0(\epsilon),\epsilon}, \eta_j) \\ &\leq \left| \sum_{k,j} \tilde{a}_{jk}(\tilde{u}_k, \eta_j) - \tilde{a}_{jk}^{\beta_0(\epsilon),\epsilon}(\Pi_k^{\beta_0(\epsilon)} \tilde{u}^{\beta_0(\epsilon),\epsilon}, \eta_j) \right| + \left| \sum_{k,j} \tilde{a}_{jk}(\Pi_k^{\beta_0(\epsilon)} \tilde{u}^{\beta_0(\epsilon),\epsilon}, \eta_j) - \tilde{a}_{jk}^{\beta_0(\epsilon),\epsilon}(\Pi_k^{\beta_0(\epsilon)} \tilde{u}^{\beta_0(\epsilon),\epsilon}, \eta_j) \right| \\ &= \left| \sum_j (\tilde{f}_j - \tilde{f}_j^{\beta_0(\epsilon),\epsilon}, \eta_j) \right| + \left| \sum_{k,j} \tilde{a}_{jk}(\Pi_k^{\beta_0(\epsilon)} \tilde{u}^{\beta_0(\epsilon),\epsilon}, \eta_j) - \tilde{a}_{jk}^{\beta_0(\epsilon),\epsilon}(\Pi_k^{\beta_0(\epsilon)} \tilde{u}^{\beta_0(\epsilon),\epsilon}, \eta_j) \right| \end{aligned}$$

and

$$\left(\sum_k \|\eta_k\|_{\tilde{V}_k}^2 \right)^{\frac{1}{2}} \leq \frac{|\sum_j (\tilde{f}_j - \tilde{f}_j^{\beta_0(\epsilon),\epsilon}, \eta_j)| + |\sum_{k,j} \tilde{a}_{jk}(\Pi_k^{\beta_0(\epsilon)} \tilde{u}^{\beta_0(\epsilon),\epsilon}, \eta_j) - \tilde{a}_{jk}^{\beta_0(\epsilon),\epsilon}(\Pi_k^{\beta_0(\epsilon)} \tilde{u}^{\beta_0(\epsilon),\epsilon}, \eta_j)|}{\left(\sum_k \|\eta_k\|_{\tilde{V}_k}^2 \right)^{\frac{1}{2}} \left(\sum_j \|\tilde{f}_j\|_{L^2(\Omega)}^2 \right)^{\frac{1}{2}}} \rightarrow 0.$$

This completes the proof. \square

3.2. Two examples. In this section, we present two examples. By the decaying property of the function $\phi_j^{h,\epsilon}$, we have $\kappa_{j,k}(x, z) = 0$ if $x \neq z$.

Case 1: We take $\kappa(\epsilon, x) = \kappa\left(\frac{x}{\epsilon}\right)$, $\psi_1^{h,\epsilon}(x, y) = \frac{1}{|K(x)|^{\frac{1}{2}}} I_{K(x)}(y)$ and $\tilde{\kappa}^\epsilon = 1$. Then we have

$$\tilde{u}_1^{\epsilon^{\frac{1}{2}},\epsilon} \rightarrow u_0^*$$

where $\int_{\Omega} \kappa^* \nabla u_0^* \cdot \nabla v dx = \int_{\Omega} f v$ and we deduce from Theorem 1 that

$$\tilde{a}_{jk}^{\epsilon^{\frac{1}{2}},\epsilon}(u, v) \rightarrow \int_{\Omega} \kappa^* \nabla u \cdot \nabla v dx, \quad \text{as } \epsilon \rightarrow 0.$$

Case 2: We take $\kappa(\epsilon, x) = \kappa_0(x) + \kappa_1\epsilon^{-1}I_{\Gamma(\epsilon)}$ where $\Gamma(\epsilon) = \{x \in \Omega \mid d(x, \Gamma) < \epsilon\}$ and Γ is a fracture in the domain Ω , and

$$\psi_1^{h,\epsilon}(x, y) = \frac{1}{|K(x) \setminus F(\epsilon)|^{\frac{1}{2}}} I_{K(x) \setminus F(\epsilon)}(y), \quad \psi_2^{h,\epsilon}(x, y) = \frac{1}{|K(x) \cap F(\epsilon)|^{\frac{1}{2}}} I_{K(x) \cap F(\epsilon)}(y).$$

If $u^\epsilon \rightarrow u^0$ in $H^1(\Omega)$ and $u^\epsilon|_\Gamma \rightarrow u_\Gamma^0$ in $H^1(\Gamma)$, we again deduce from Theorem 1 that

$$\begin{aligned} \tilde{a}_{11}^{\epsilon,\epsilon}(u, v) &\rightarrow \int_\Omega \kappa_0 \nabla u \cdot \nabla v dx + h^{-1} \int_\Gamma Q uv + O(h), \\ \tilde{a}_{12}^{\epsilon,\epsilon}(u, v) &\rightarrow -h^{-1} \int_\Gamma Q uv + O(h), \\ \tilde{a}_{21}^{\epsilon,\epsilon}(u, v) &\rightarrow -h^{-1} \int_\Gamma Q uv + O(h), \\ \tilde{a}_{22}^{\epsilon,\epsilon}(u, v) &\rightarrow \int_\Gamma \kappa_1 \nabla_\Gamma u \cdot \nabla_\Gamma v + h^{-1} \int_\Gamma Q uv + O(h). \end{aligned}$$

Hence we obtain the following upscale system

$$\begin{aligned} \int_\Omega \kappa_0^* \nabla u_1 \cdot \nabla v + h^{-1} \int_\Gamma Q(u_1 - u_2)v + O(h) &= \int_\Omega \tilde{f}_1 v, \quad \forall v \in H^1(\Omega), \\ \int_\Gamma \kappa_0^* \nabla_\Gamma u_2 \cdot \nabla_\Gamma v + h^{-1} \int_\Gamma Q(u_2 - u_1)v + O(h) &= \int_\Gamma \tilde{f}_2 v, \quad \forall v \in H^1(\Gamma). \end{aligned}$$

We remark that the operator Q is defined in the limit above.

3.3. RVE approximation. In this section, we will discuss using a RVE concept to approximate the bilinear operator $\tilde{a}_{jk}^{h,\epsilon}$. Since $\tilde{a}_{jk}^{h,\epsilon}(u, v) := \int_\Omega \int_\Omega v(y) \tilde{\kappa}^\epsilon(y) \tilde{\kappa}_{jk}^{h,\epsilon}(x, y) \tilde{\kappa}^\epsilon(x) u(x)$, we can approximate $\tilde{a}_{jk}^{h,\epsilon}$ by using a suitable quadrature rule for the integral. For each coarse grid element $K \in \mathcal{T}_H$, we consider there is a set of RVEs, $K_{REV,k}$. We will approximate $\tilde{a}_{jk}^{h,\epsilon}$ by \tilde{a}_{jk}^{RVE} such that

$$(3.5) \quad \tilde{a}_{jk}^{RVE} = \sum_k \omega_{RVE,k} \int_{K_{REV,k}} \int_{K_{REV,k}} v(y) \tilde{\kappa}^\epsilon(y) \tilde{\kappa}_{jk}^{h,\epsilon}(x, y) \tilde{\kappa}^\epsilon(x) u(x).$$

4. NUMERICAL RESULTS

In this section, we will consider a numerical example to demonstrate the performance of the method. The computational domain Ω is defined as $\Omega = [0, 1]^2$. The medium parameter κ_ϵ is defined as

$$\kappa_\epsilon = \begin{cases} \frac{3}{10\epsilon} & \text{if } x \in \Gamma_1^\epsilon \setminus \Gamma_2^\epsilon \\ \frac{1}{\epsilon} & \text{if } x \in \Gamma_2^\epsilon \cup \Gamma_3^\epsilon \\ \frac{7}{10\epsilon} & \text{if } x \in \Gamma_4^\epsilon \\ 1 & \text{if } x \in \Omega \setminus (\Gamma_1^\epsilon \cup \Gamma_2^\epsilon \cup \Gamma_3^\epsilon \cup \Gamma_4^\epsilon) \end{cases}$$

where

$$\begin{aligned} \Gamma_1^\epsilon &= \{x \mid |x_1 - \frac{1}{2}| < \epsilon, \frac{1}{4} < x_2 < \frac{7}{8}\}, \\ \Gamma_2^\epsilon &= \{x \mid \left| \frac{x_1 + x_2 - 1}{\sqrt{2}} \right| < \epsilon, -\frac{1}{4} < x_1 - x_2 < \frac{3}{4}\}, \\ \Gamma_3^\epsilon &= \{x \mid \left| \frac{2x_1 - 3x_2 + 0.2}{\sqrt{13}} \right| < \epsilon, \frac{7}{8} < \frac{3x_1 + 2x_2}{\sqrt{13}} < \frac{9}{8}\}, \\ \Gamma_4^\epsilon &= \{x \mid \sqrt{2} \left| (x_1 - \frac{1}{2})^2 + (x_2 - \frac{1}{2})^2 - \frac{1}{8} \right| < \epsilon, x_1 < \frac{1}{2}, x_2 < \frac{3}{4}\}. \end{aligned}$$

The choice of the RVE location is illustrated in Figure 4.1. The source term f is defined as

$$f(x) = e^{-40((x_1 - \frac{9}{10})^2 + (x_2 - \frac{1}{10})^2)}.$$

In Figure 4.2, we present the computational results. In the first figure (left plot in Figure 4.2), we present the reference solution. In the second figure (middle plot in Figure 4.2), we present the matrix part of the upscaled solution. In the third figure (right plot in Figure 4.2), we present the channel part of the upscaled solution. From these results, we observe that our proposed upscaling method is able to produce accurate upscaled solutions.

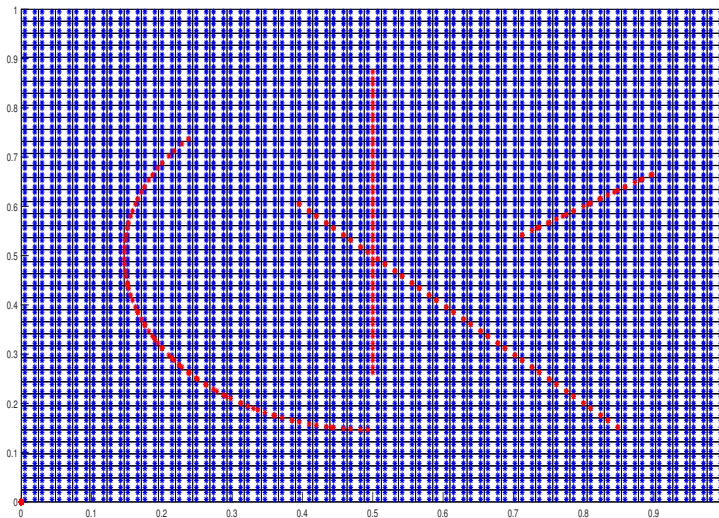


FIGURE 4.1. The computational domain Ω , the medium parameter κ_ϵ and the RVE points.

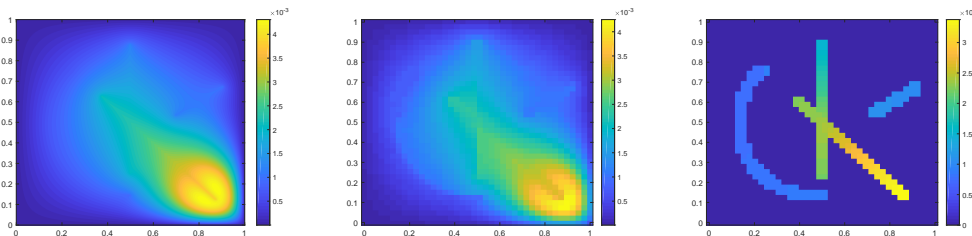


FIGURE 4.2. Computational results for the first example. Left: reference solution, Middle: upscaled solution (matrix), Right: upscaled solution (channel).

In the next example, we will consider a time dependent case. We assume u_1 and u_2 satisfy the following equations

$$(4.1) \quad \left(\left(\Pi_i^h(u_i)(\cdot, t) \right)_t, \Pi_i^h(v_i) \right) + \sum_j \tilde{a}_{ij}(u_j, v_i) = \int_{\Omega} f v_i, \quad \forall v_i \in V_i, \quad \forall t \in (0, T].$$

The computational domain Ω is defined as $\Omega = [0, 1]^2$. The medium parameter κ_ϵ is defined as

$$\kappa_\epsilon = \begin{cases} 10 & \text{if } \left| \sin\left(\frac{\pi((1-x_2)x_2 + x_1)}{\epsilon}\right) \sin\left(\frac{\pi(x_2 + x_1^2)}{\epsilon}\right) \right| < 0.2, \\ \frac{\epsilon}{10000} & \text{otherwise.} \end{cases}$$

The source term f is chosen to be the same as the previous example. In Figure 4.3, we illustrate the medium parameter κ_ϵ and the RVE points. In the top figure, we present the computational domain, coarse grid and the RVE points. In the bottom left figure, we present the medium parameter κ_ϵ around the point $(0.0717, 0.717)$. In the bottom middle and bottom right figures, we present the medium parameter κ_ϵ around the points $(0.5262, 0.5262)$ and $(0.9808, 0.717)$ respectively.

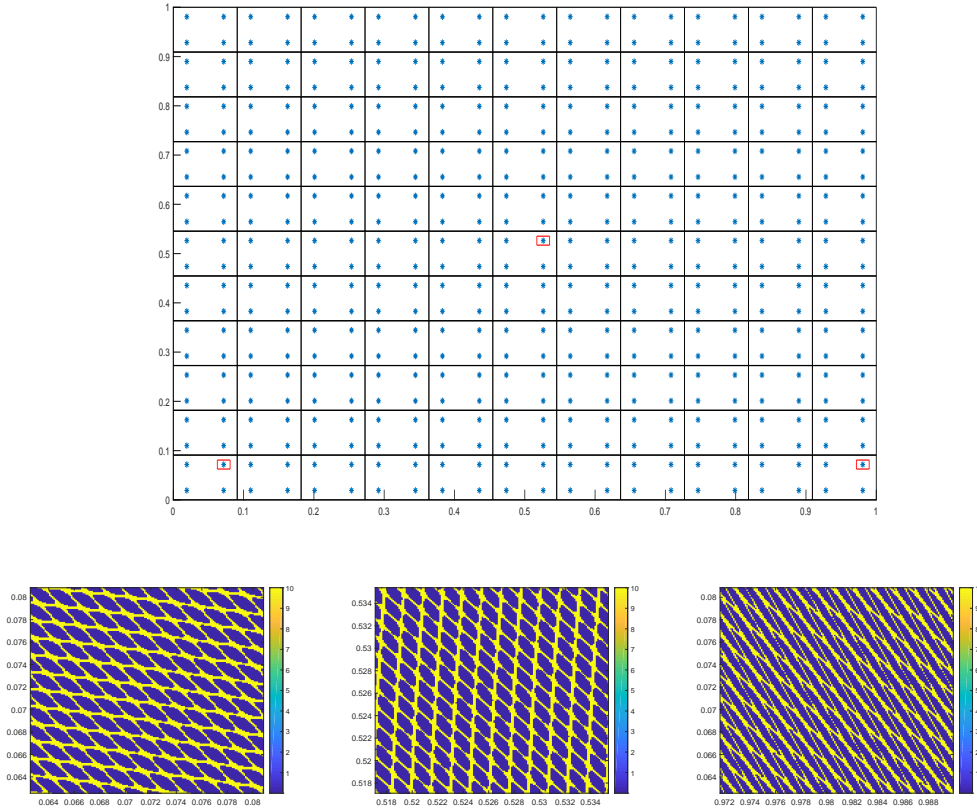


FIGURE 4.3. The RVE points and the medium parameter κ_ϵ for the second example. Top: RVE points in the domain. Bottom Left: κ_ϵ around $(0.0717, 0.717)$. Bottom Middle: κ_ϵ around $(0.5262, 0.5262)$. Bottom Right: κ_ϵ around $(0.9808, 0.717)$.

In Figure 4.4, we present the computational results for the second example. In the three figures on the top, we present the matrix part of the upscaled solutions at the times $T = 0.005$, $T = 0.01$ and $T = 0.02$ respectively. In the three figures at the bottom, we present the channel part of the upscaled solutions at the times $T = 0.005$, $T = 0.01$ and $T = 0.02$ respectively.

4.1. Nonlinear example with machine learning. In this section, we present numerical results for the proposed method. Our examples use some of the tools developed in [31, 40]. The goal of this example is to use machine learning to compute macroscale parameters based on RVE simulations. The method is similar to our previous approach [31, 40]; however, the calculations are performed in RVEs.

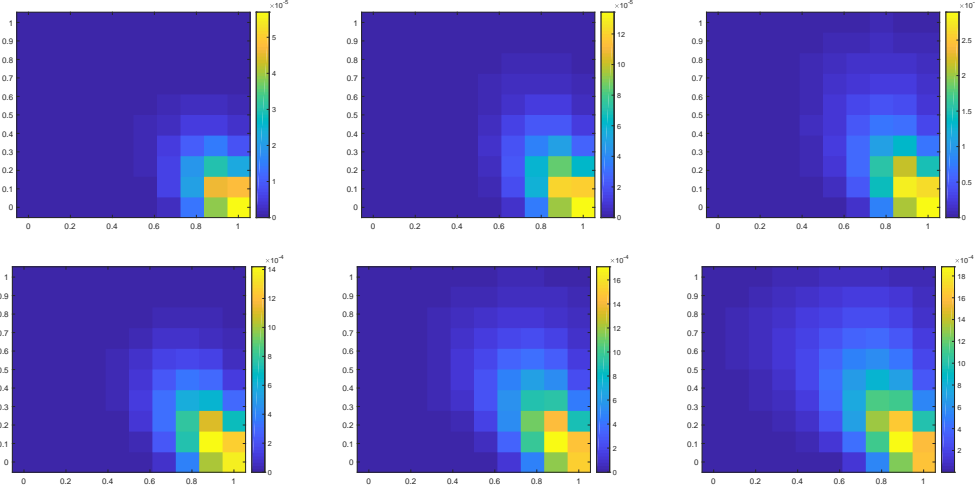


FIGURE 4.4. Computational results for the second example. Top Left: upscaled solution at $T = 0.005$ (matrix), Top Middle: upscaled solution at $T = 0.01$ (matrix), Top Right: upscaled solution at $T = 0.02$ (matrix), Bottom Left: upscaled solution at $T = 0.005$ (channel), Bottom Middle: upscaled solution at $T = 0.01$ (channel), Bottom Right: upscaled solution at $T = 0.02$ (channel).

We consider nonlinear flow problem (unsaturated flow problem) in fractured media $\Omega = [0, 1] \times [0, 1]$ with no flux boundary conditions. We set source terms $q_f = 10^5$ in the fracture continuum in $[0.95, 1.0] \times [0.95, 1.0]$. We use 10×10 coarse grid. For the nonlinear coefficient, we use $k^\alpha(x, u) = k_r(u)k_s^\alpha(x)$ with $k_r(u) = \exp(-a|u|)$, $a = 0.1$ ($\alpha = m, f$). We set $c^m = 1$, $c^f = 1$, $k_s^f = 10^3$, $k_m = 1$ and $T_{max} = 0.025$ with 50 time steps. The numerical calculations of the effective properties has been implemented with the open-source finite element software PETSc and FEniCS [32, 33, 2]. Machine Learning algorithm is implemented using Keras library.

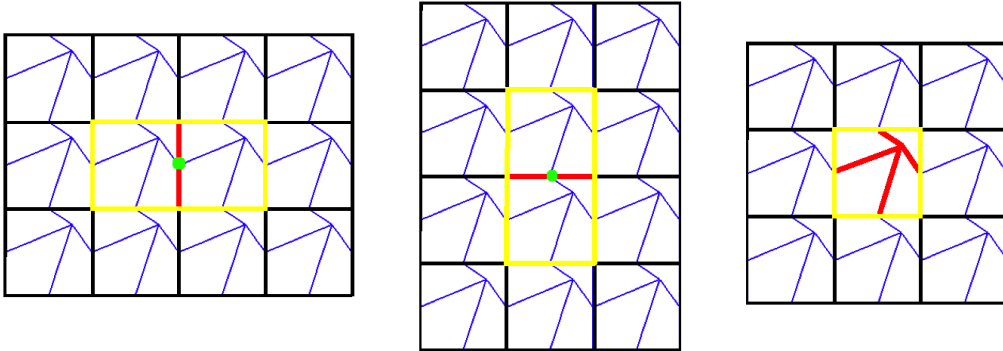


FIGURE 4.5. Local domains to generate datasets. Left: NN_1 (T^{mm} on edge (red color)) and NN_4 (T^{ff} on point (green color)). Middle: NN_2 (T^{mm} on edge (red color)) and NN_5 (T^{ff} on point (green color)). Right: NN_3 (T^{mf} on fracture interface (red color)).

Each sample X_l contains information about coarse grid solution in oversampled local domain

$$X_l = (X_{l+}^m, X_{l+}^f),$$

	MSE	RMSE (%)	MAE (%)
NN_1	0.0358	1.8929	1.5824
NN_2	0.0895	2.9930	2.4455
NN_3	0.0006	0.2544	0.2309
NN_4	0.0163	1.2801	1.2313
NN_5	0.0114	1.0686	0.9461

TABLE 1. Learning performance of machine learning algorithm

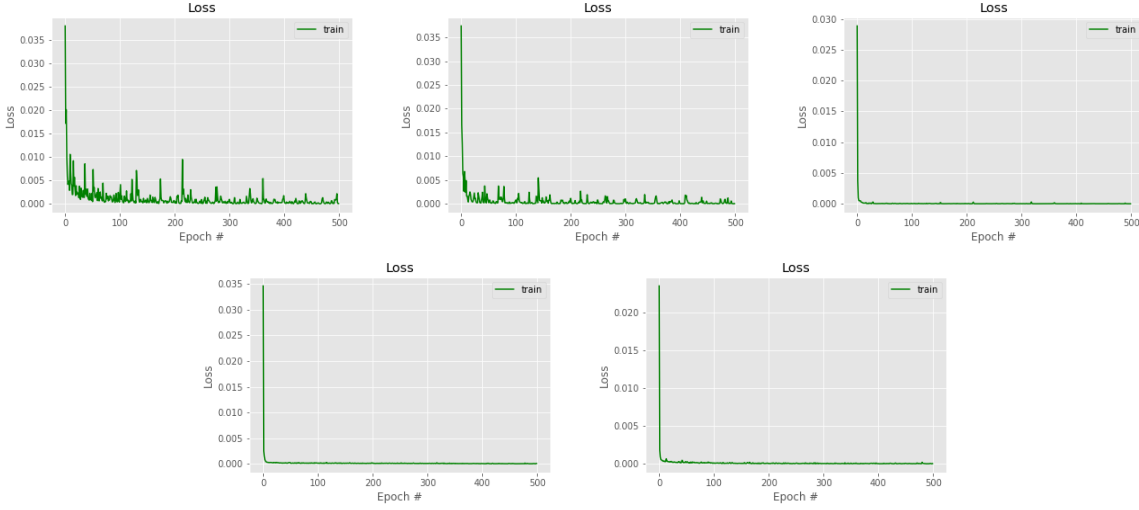


FIGURE 4.6. Learning performance of machine learning algorithm. Loss functions. Left: NN_1 (T^{mm}) and NN_4 (T^{ff}). Left: NN_2 (T^{mm}) and NN_5 (T^{ff}). Left: NN_3 (T^{mf}).

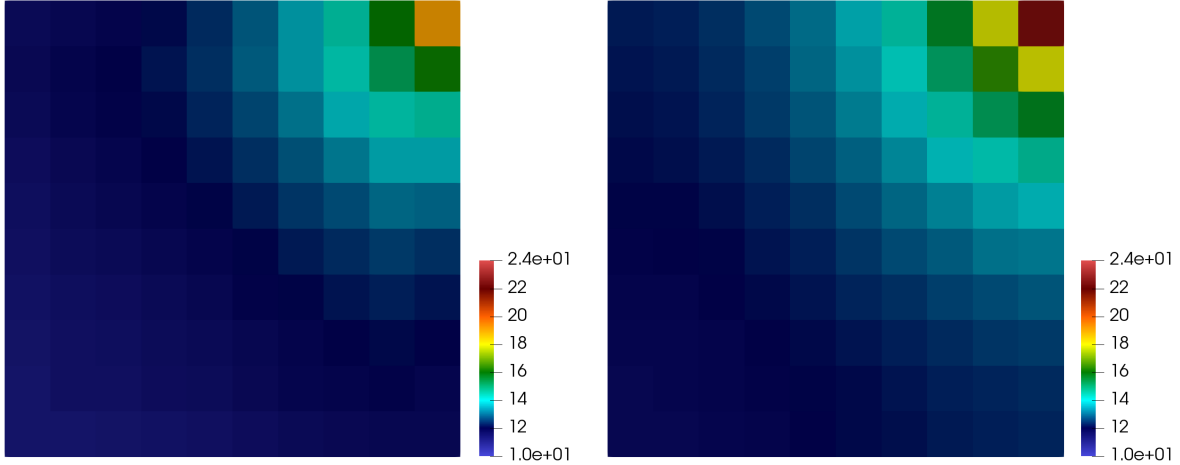


FIGURE 4.7. Solution on final time t_m , $m = 50$. Left: u_m . Right: u_f

and output

$$Test\ 1: Y_l = (T_l^{\alpha\beta, NL}), \quad \alpha, \beta = m, f.$$

For the training of the neural networks, we use a dataset generated via solution of the local problems in oversamples local domains (see Figure 4.5). We train four neural networks for each type of transmissibility: NN_1 for horizontal coarse edges for matrix-matrix flow, NN_2 for vertical coarse edges for matrix-matrix flow, NN_3 for matrix - fracture flow and NN_4 and NN_5 for fracture - fracture flow (Figure 4.5). For calculations, we use 500 epochs with a batch size $N_b = 100$ and Adam optimizer with learning rate $\epsilon = 0.001$. For accelerating of the training process of the multi-input CNN, we use GPU (GeForce GTX 1060). We use 3×3 convolutions with RELU activation. For each input data, we have 3 layers of CNN with two final fully connected layer. Convolution layer contains 4, 8 and 16 feature maps. We use dropout with rate 10 % in each layer in order to prevent over-fitting. Finally, we combine CNN output and perform three additional fully connected layers with size 200, 50 and 1(one final output). Presented algorithm is used to learn dependence between multi-input data and upscaled nonlinear transmissibilities.

For error calculation on the dataset, we used mean square errors, relative mean absolute and relative root mean square errors

$$MSE = \sum_i |Y_i - \tilde{Y}_i|^2, \quad RMSE = \sqrt{\frac{\sum_i |Y_i - \tilde{Y}_i|^2}{\sum_i |Y_i|^2}}, \quad MAE = \frac{\sum_i |Y_i - \tilde{Y}_i|}{\sum_i |Y_i|},$$

where Y_i and \tilde{Y}_i denotes reference and predicted values for sample X_i . Learning performance for neural networks are presented in Table 1. Loss function (MSE) is presented in Figure 4.6. We observe a good convergence with small error for each neural network. In Figure 4.7, we depict solution of the problem, u_m and u_f .

ACKNOWLEDGEMENTS

The research of Eric Chung is partially supported by the Hong Kong RGC General Research Fund (Project numbers 14304217 and 14302018) and CUHK Faculty of Science Direct Grant 2018-19. YE would like to thank the partial support from NSF 1620318. YE would also like to acknowledge the support of Mega-grant of the Russian Federation Government (N 14.Y26.31.0013)

REFERENCES

- [1] A. Abdulle and B. Engquist. Finite element heterogeneous multiscale methods with near optimal computational complexity. *SIAM J. Multiscale Modeling and Simulation*, 6(4):1059–1084, 2007.
- [2] Satish Balay, Kris Buschelman, Victor Eijkhout, William D Gropp, Dinesh Kaushik, Matthew G Knepley, Lois Curfman McInnes, Barry F Smith, and Hong Zhang. Petsc users manual. Technical report, Technical Report ANL-95/11-Revision 2.1. 5, Argonne National Laboratory, 2004.
- [3] Donald L Brown, Yalchin Efendiev, and Viet Ha Hoang. An efficient hierarchical multiscale finite element method for stokes equations in slowly varying media. *Multiscale Modeling & Simulation*, 11(1):30–58, 2013.
- [4] Eric Cances, Virginie Ehrlicher, Frédéric Legoll, and Benjamin Stamm. An embedded corrector problem to approximate the homogenized coefficients of an elliptic equation. *Comptes Rendus Mathématique*, 353(9):801–806, 2015.
- [5] Jie Chen, Shuyu Sun, and Zhengkang He. Homogenize coupled stokes–cahn–hilliard system to darcy’s law for two-phase fluid flow in porous medium by volume averaging. *Journal of Porous Media*, 22(1), 2019.
- [6] Jie Chen, Shuyu Sun, and Xiaoping Wang. Homogenization of two-phase fluid flow in porous media via volume averaging. *Journal of Computational and Applied Mathematics*, 353:265–282, 2019.
- [7] E. Chung, Y. Efendiev, and C. Lee. Mixed generalized multiscale finite element methods and applications. *SIAM Multiscale Model. Simul.*, 13:338–366, 2014.
- [8] E. Chung, Y. Efendiev, and W. T. Leung. Generalized multiscale finite element method for wave propagation in heterogeneous media. *SIAM Multiscale Model. Simul.*, 12:1691–1721, 2014.
- [9] Eric Chung, Yalchin Efendiev, and Wing Tat Leung. Constraint energy minimizing generalized multiscale finite element method in the mixed formulation. *Computational Geosciences*, 22(3):677–693, 2018.
- [10] Eric T Chung, Efendiev, Wing Tat Leung, Maria Vasilyeva, and Yating Wang. Non-local multi-continua upscaling for flows in heterogeneous fractured media. *arXiv preprint arXiv:1708.08379*, 2018.
- [11] Eric T Chung, Yalchin Efendiev, Wing T Leung, and Mary Wheeler. Nonlinear nonlocal multicontinua upscaling framework and its applications. *International Journal for Multiscale Computational Engineering*, 16(5), 2018.
- [12] Eric T Chung, Yalchin Efendiev, and Wing Tat Leung. Constraint energy minimizing generalized multiscale finite element method. *Computer Methods in Applied Mechanics and Engineering*, 339:298–319, 2018.
- [13] Eric T Chung, Yalchin Efendiev, and Wing Tat Leung. Fast online generalized multiscale finite element method using constraint energy minimization. *Journal of Computational Physics*, 355:450–463, 2018.

- [14] Eric T Chung, Wing Tat Leung, and Sara Pollock. Goal-oriented adaptivity for GMsFEM. *Journal of Computational and Applied Mathematics*, pages 625–637, 2015.
- [15] W. E and B. Engquist. Heterogeneous multiscale methods. *Comm. Math. Sci.*, 1(1):87–132, 2003.
- [16] Y. Efendiev, J. Galvis, and T. Y. Hou. Generalized multiscale finite element methods (gmsfem). *Journal of Computational Physics*, 251:116–135, 2013.
- [17] Dimitrios Fafalis and Jacob Fish. Computational continua for linear elastic heterogeneous solids on unstructured finite element meshes. *International Journal for Numerical Methods in Engineering*, 115(4):501–530, 2018.
- [18] Jacob Fish and Sergey Kuznetsov. Computational continua. *International Journal for Numerical Methods in Engineering*, 84(7):774–802, 2010.
- [19] Jacob Fish and Zheng Yuan. Multiscale enrichment based on partition of unity. *International Journal for Numerical Methods in Engineering*, 62(10):1341–1359, 2005.
- [20] Shubin Fu, Eric Chung, and Guanglian Li. Edge multiscale methods for elliptic problems with heterogeneous coefficients. *Journal of Computational Physics*, 2019.
- [21] Kai Gao, Shubin Fu, Richard L Gibson Jr, Eric T Chung, and Yalchin Efendiev. Generalized multiscale finite-element method (gmsfem) for elastic wave propagation in heterogeneous, anisotropic media. *Journal of Computational Physics*, 295:161–188, 2015.
- [22] H. Hajibeygi, D. Kavounis, and P. Jenny. A hierarchical fracture model for the iterative multiscale finite volume method. *Journal of Computational Physics*, 230(4):8729–8743, 2011.
- [23] Patrick Henning, Axel Malqvist, and Daniel Peterseim. A localized orthogonal decomposition method for semi-linear elliptic problems. *arXiv preprint arXiv:1211.3551*, 2012.
- [24] V.H. Hoang and C. Schwab. High dimensional finite elements for elliptic problems with multiple scales. *SIAM Multiscale Modeling and Simulation*, 3:168–194, 2004.
- [25] T. Hou and X.H. Wu. A multiscale finite element method for elliptic problems in composite materials and porous media. *J. Comput. Phys.*, 134:169–189, 1997.
- [26] P. Jenny, S.H. Lee, and H. Tchelepi. Multi-scale finite volume method for elliptic problems in subsurface flow simulation. *J. Comput. Phys.*, 187:47–67, 2003.
- [27] P. Jenny, S.H. Lee, and H. Tchelepi. Adaptive multi-scale finite volume method for multi-phase flow and transport in porous media. *SIAM J. Multiscale Modeling and Simulation*, 3:30–64, 2004.
- [28] V. V. Jikov, S. M. Kozlov, and O. A. Oleinik. *Homogenization of Differential Operators and Integral Functionals*. Springer-Verlag, 1991.
- [29] Claude Le Bris, Frédéric Legoll, and Alexei Lozinski. An msfem type approach for perforated domains. *Multiscale Modeling & Simulation*, 12(3):1046–1077, 2014.
- [30] Claude Le Bris, Frédéric Legoll, and Florian Thomines. Multiscale finite element approach for weakly random problems and related issues. *ESAIM: Mathematical Modelling and Numerical Analysis*, 48(3):815–858, 2014.
- [31] Wing T Leung, Eric T Chung, Yalchin Efendiev, Maria Vasilyeva, and Mary Wheeler. Space-time nonlinear upscaling framework using non-local multi-continuum approach. *arXiv preprint arXiv:1908.05582*, to appear in *International Journal of Multiscale Engineering*, 2019.
- [32] Anders Logg, Kent-Andre Mardal, and Garth Wells. *Automated solution of differential equations by the finite element method: The FEniCS book*, volume 84. Springer Science & Business Media, 2012.
- [33] Anders Logg, Kent-Andre Mardal, and Garth Wells. *Automated solution of differential equations by the finite element method: The FEniCS book*, volume 84. Springer Science & Business Media, 2012.
- [34] H. Owhadi and L. Zhang. Metric-based upscaling. *Comm. Pure. Appl. Math.*, 60:675–723, 2007.
- [35] A.J. Roberts and I. Kevrekidis. General tooth boundary conditions for equation free modeling. *SIAM J. Sci. Comput.*, 29(4):1495–1510, 2007.
- [36] Amgad Salama, Shuyu Sun, Mohamed F El Amin, Yi Wang, and Kundan Kumar. Flow and transport in porous media: A multiscale focus. *Geofluids*, 2017, 2017.
- [37] G. Samaey, I.G. Kevrekidis, and D. Roose. Patch dynamics with buffers for homogenization problems. *J. Comput. Phys.*, 213(1):264–287, 2006.
- [38] G. Samaey, D. Roose, and I.G. Kevrekidis. The gap-tooth scheme for homogenization problems. *SIAM J. Multiscale Modeling and Simulation*, 4(1):278–306, 2005.
- [39] Wee Chin Tan and Viet Ha Hoang. High dimensional finite element method for multiscale nonlinear monotone parabolic equations. *Journal of Computational and Applied Mathematics*, 345:471–500, 2019.
- [40] Maria Vasilyeva, Wing T Leung, Eric T Chung, Yalchin Efendiev, and Mary Wheeler. Learning macroscopic parameters in nonlinear multiscale simulations using nonlocal multicontinua upscaling techniques. *arXiv preprint arXiv:1907.02921*, 2019.

DEPARTMENT OF MATHEMATICS, THE CHINESE UNIVERSITY OF HONG KONG, SHATIN, NEW TERRITORIES, HONG KONG SAR, CHINA

DEPARTMENT OF MATHEMATICS, TEXAS A&M UNIVERSITY, COLLEGE STATION, TX 77843, USA
E-mail address: efendiev@math.tamu.edu

ICES, UNIVERSITY OF TEXAS, AUSTIN, TX, USA

INSTITUTE FOR SCIENTIFIC COMPUTATION, TEXAS A&M UNIVERSITY, COLLEGE STATION, TX, USA & MULTISCALE MODEL REDUCTION LABORATORY, NORTH-EASTERN FEDERAL UNIVERSITY, YAKUTSK, RUSSIA